RSC Advances

PAPER

View Article Online
View Journal | View Issue

Cite this: *RSC Adv.*, 2023, **13**, 35445

Ceria nanomaterials containing ytterbium: low and high concentration – luminescence analyzed in the near infrared region†

Sitshengisiwe Chemura,[a] Tim Schrumpf,[a] Christina Günter[b] and Michael U. Kumke *[a]

Lanthanide based ceria nanomaterials are important practical materials due to the redox properties that are useful in the avenues pertaining to technology and life sciences. Sub 10 nm spherical and highly monodisperse $Ce_{1-x}Yb_xO_{2-y}$ ($0.04 \leq x \leq 0.22$) nanoparticles were synthesized by thermal decomposition, annealed separately at 773 K and 1273 K for 2 hours and characterized. Elemental mapping for Yb^{3+} doped ceria nanoparticles shows homogeneous distribution of Yb^{3+} atoms in the ceria with low Yb^{3+} content annealed at 773 K and 1273 K for 2 hours. However, clusters are observed for 773 K annealed ceria samples with high concentration of Yb^{3+}. These clusters are not detected in 1273 K annealed nanomaterials. Introducing small amounts of Yb^{3+} ions into the ceria lattice as spectroscopic probes can provide detailed information about the atomic structure and local environments allowing the monitoring of small structural changes, such as clustering. The emission spectra observed at room temperature and at 4 K have a manifold of bands that corresponds to the $^2F_{5/2} \rightarrow {}^2F_{7/2}$ transition of Yb^{3+} ions. Some small shifts are observed in the Stark splitting pattern depending on the sample and the annealing conditions. The deconvolution by PARAFAC analysis yielded luminescence decay kinetics as well as the associated luminescence spectra of three species for each of the low Yb^{3+} doped ceria samples annealed at 773 K and one species for the 1273 K annealed samples. However, the ceria samples with high concentration of Yb^{3+} annealed at the two temperatures showed only one species with lower decay times as compared to the low Yb^{3+} doped ceria samples.

Received 9th October 2023
Accepted 26th November 2023

DOI: 10.1039/d3ra06868d

rsc.li/rsc-advances

Introduction

Ceria, CeO_2, is one of the most important materials in industrial applications: in solid oxide fuel cells, in biomedical applications, and as heterogeneous catalysts.[1–5] Modifying the structure of pure CeO_2 through doping (or mixing) with lanthanide ions (Ln^{3+}) or tetravalent ions increases its lattice oxygen mobility. This in turn modifies the redox properties of the oxide.[6,7] CeO_2 can be easily altered by doping with other rare-earth ions for example Yb^{3+}, because of their comparable ionic radii. Yb^{3+} has an ionic radius of 0.0985 nm which is close to that of Ce^{4+} (0.0970 nm) and Ce^{3+} (0.1143 nm).[4,8–10] During the modification process of the crystal lattice, the incorporation of the Yb^{3+} or other lanthanides ions results in the Ce^{4+} ions substitution.[1] The consequence is a one charge-compensating oxygen vacancy for every two trivalent dopants, resulting in multifaceted possible arrangements between Ce^{4+}, Ln^{3+}, O^{2-} and oxygen vacancies.[7,11,12] Yb^{3+} doped in nanomaterials finds many applications such as sensitizer in up-conversion and also as luminescence probe showing near infra-red (NIR) emission.[13,14] Like other Ln^{3+} ions, Yb^{3+} can exhibit sharp luminescence bands *via* intra-4f or 4f–5d transitions.[15] Taking advantage of this noble property, Yb^{3+} doped nanomaterials are an integral part of many lasers.[16–19] With Yb^{3+} doping, highly desired imaging in the NIR spectral range is enabled which is otherwise hardly possible with other materials.[1] The preferred oxidation state of ytterbium is +III (f^{13}), but the +II (f^{14}) can also be formed. Depending on its oxidation state f–f transitions or f–d-transitions can be observed. In complexes and solids Yb^{3+} ions can be found in different local symmetries, for example during formation of ceria, some of the Yb^{3+} ions substitute for the Ce ions and situate themselves in cubic (O_h), tetragonal (C_{4v}), or trigonal C_{3v} environments. These three sites can be accurately detected optically and only at very low dopant concentrations as there are no complex centers and defects in the lattices, which occur as a result of aggregates of Yb^{3+} ions when they are present in higher concentrations.[20] Thus, at high concentrations an exclusive type of Yb^{3+} luminescent center is

[a]*Institute of Chemistry (Optical Sensing and Spectroscopy), University of Potsdam, Karl-Liebknecht-Str. 24-25, 14476 Potsdam, Germany. E-mail: kumke@uni-potsdam.de*

[b]*Institute for Earth Sciences, University of Potsdam, Karl-Liebknecht-Str. 24-25, 14476 Potsdam, Germany*

† Electronic supplementary information (ESI) available: SEM images and additional TEM images (SI1 and SI2). See DOI: https://doi.org/10.1039/d3ra06868d

formed which dominates the emission. This has also been reported for CaF_2:Yb^{3+} nanomaterials.[21–23]

The Yb^{3+} ion has the electronic ground and excited states assigned to the $^2F_{7/2}$ and $^2F_{5/2}$ state, respectively.[24,25] Depending on the crystal field, these can be further split into Stark level multiplets. At a low C_s symmetry, the ground state $^2F_{7/2}$ can split into four and the excited state $^2F_{5/2}$ into three Kramer's doublets.[16,20,25–27] Thus, the transitions between the splitting levels are sensitive to the lattice site environment and also to the thermal vibration of crystal lattice occurring at room temperature and therefore thermal processes play a crucial part on the optical properties of the system.[19,25,28]

Trivalent rare-earth ions doped nanomaterials have a tendency to form cluster structures that contain at least two rare-earth ions in close environments and that are luminescence quenching centers.[20] An additional luminescence quenching process can occur as a result of internal defects inside the oxide lattice, *e.g.*, of CeO_2, when Yb^{3+} are available in the lattice at high concentrations.[1] Yb^{3+} clusters can likewise act as trapping centers resulting in a fast-non-radiative decay.[29,30] Additionally, luminescence quenching takes place through cooperative luminescence between Yb^{3+}–Yb^{3+} pairs. Annealing nanoparticles containing Yb^{3+} ions results in improved crystalline structure and to a greater extent eliminates quenching centers resulting in intensification of high temperature annealed samples' NIR emission.[17] With the Gd_2O_3:Yb^{3+} phosphor, luminescence intensity was observed to become higher with increasing annealing temperature.[27] This is envisaged to be due to lattice distortion which is eliminated by heating to a higher temperature and promoting crystallite growth, which in turn is responsible for the enhancement of NIR emission. Annealing Yb^{3+} doped CaF_2 crystals in inert atmosphere also resulted in the reduction of Yb^{3+} to Yb^{2+} energy transfer and this also reported for $BaZrO_3$:Yb^{3+} after a calcination at 1273 K.[17]

Upconversion luminescence has been used to track Yb^{3+} distribution in a ceria lattice incorporated with other lanthanide ions and corroborate the data from XRD and Raman on the formation of homogeneous solid solutions.[29] In these materials, the down conversion luminescence of Yb^{3+} is seldom examined. Instead, the luminescence of the activator ions (Er^{3+}, Tm^{3+} or Ho^{3+}) is detected.

In this work, the luminescence of Yb^{3+} ions in ceria-based mixed oxides $Ce_{1-x}Yb_xO_2$ was investigated using time-resolved laser fluorescence spectroscopy (TRLFS). The dependence of the luminescence on the concentration of Yb^{3+} ions in ceria and on annealing temperatures was examined. The TRLFS experiments were carried out at room temperature and at 4 K (cryogenic conditions) in order to elucidate the distribution of Yb^{3+} ion in the ceria lattice, *e.g.*, with respect the presence of lattice defects or to clustering.

Experimental section

$Ce_{1-x}Yb_xO_2$ nanomaterial synthesis

Thermal decomposition method was used to synthesize ceria nanoparticles doped (low content) or mixed (high content) with ytterbium. The protocol from Lee *et al.* was used with modifications.[31] Briefly, ytterbium(III) nitrate pentahydrate, 99.9% (0.03 mmol; 0.0135 g), cerium(III) nitrate hexahydrate, 99.9% (0.97 mmol; 0.4212 g) were dissolved in oleylamine, technical grade, 70% (0.990 mL; 0.805 g) and 1-octadecene, technical grade, 90% (5 mL; 4 g). All chemicals were procured from Sigma-Aldrich and used without further purification. The mix proportions of ytterbium and cerium were varied according to the desired final product. The mixture was stirred (600 rpm and at 353 K) for 30 min under vacuum (~50 mbar) until a clear brownish yellow solution was formed. Thereafter, it was heated to 533 K to react for 2 h. After cooling to room temperature, 80 mL acetone was added to the solution and the nanoparticles were collected by centrifugation (30 min; 4500 rpm) using an Eppendorf centrifuge (Model 5804, Eppendorf, Germany). The nanoparticles were redispersed in hexane (max. 3 mL). The nanoparticles were washed three more times in the same way and finally dispersed in 10 mL hexane and stored in the fridge for further analyses. To obtain a powder, the volumes of the nanoparticle solvent were reduced in a Heidolph rotary evaporator equipped to a Heidolph vacuum pump, before being dried in an oven at 353 K for an hour. The powders were calcined in air at 773 K and 1273 K for 2 h after that (in an oven MLM VEB Electro Bad Frankenhausen, WMW AG Maschinenbau, Germany).

$Ce_{1-x}Yb_xO_2$ nanomaterial characterization

The powders were characterized by XRD, TEM, Raman spectroscopy, and TRLFS at room as well as ultra-low temperature. X-ray powder diffraction data were collected on a PANalytical Empyrean powder X-ray diffractometer in a Bragg–Brentano geometry. It is equipped with a PIXcel1D detector using Cu Kα radiation (λ = 1.54187 Å) operating at 40 kV and 40 mA. θ/θ scans were run in a 2θ range of 4–70° with step size of 0.0131° and a sample rotation time of 1 s. The diffractometer is equipped with a programmable divergence and anti-scatter slit, and a large Ni-beta filter. The detector was set to continuous mode with an active length of 3.0061°. The sizes of the crystallites were calculated using the Debye–Scherrer-equation:

$$D = \frac{K\lambda}{\beta \cos \theta} \quad (1)$$

where D is the crystallite size, $K = 0.9$; the Scherrer constant, λ = 0.15418 nm, β is the FWHM in radians and θ is the peak position in radians.

The lattice parameter a was calculated using the formulae:

$$d = \frac{\lambda}{2 \sin \theta} \quad (2)$$

$$a = d\sqrt{h^2 + k^2 + l^2} \quad (3)$$

where a is the lattice parameter, d is the inter-planar spacing, and θ is the diffraction angle of the peak with the highest intensity.

Raman spectra were recorded to examine the lattice vibrations in the nanomaterials at room temperature with an excitation source of 633 nm laser using a Raman microscope (Witec,

Alpha 300) with a grating of 2400 L mm^{-1} equipped with Andor DU401-BR-DD-352 CCD camera. 10× objective was used.

Scanning electron microscopy (SEM) and energy dispersive X-ray diffraction (EDXS) experiments were done on a JEOL JSM-6510 with a W-filament operated at 15 kV and equipped with an Oxford Instruments INCAx-act detector. Small amounts of the samples were deposited on a carbon glue pad. Prior to analysis, all samples were coated with 25 nm of carbon by vaporizing a thin carbon wire under extremely high temperatures in a vacuum chamber using a Polaron CC7650 Carbon Coater. The back scattered electron (BSE) detector was used for material contrast, the secondary electron (SEE) detector for topographic images at 15 kV. TEM measurements were done using a JEOL microscope (Model JEM 1011). The ImageJ software was used in the nanoparticle size calculation, for which 100 nanoparticles were considered in each case.

The time-resolved laser fluorescence spectroscopy (TRLFS) experiments were carried out using the box car method. The initial gate delay, Δt was set to 5 μs and the gate width was 100 μs using a slit width of 10 μm. Yb^{3+} ions were excited at λ_{ex} = 915 nm. Fluorescence line narrowing spectroscopy measurements were accomplished by cooling samples contained in NMR tubes to $T = 5$ K using a closed cycle liquid helium cryostat. The cryostat is composed of a helium compressor unit (CKW-21, Sumitomo Heavy Industries Ltd.), a vacuum pump for the sample chamber (Turbolab 80, Oerlikon Leybold Vacuum), and a temperature controller (331, Lakeshore). A pulsed Nd:YAG laser (Quanta Ray, Spectra Physics, USA) with a set repetition rate of 10 Hz was coupled to an optical parametric oscillator (OPO, GWU Lasertechnik, Germany), serving as excitation light source. The excitation light was coupled into one of the branches of a Y-shaped fiber bundle, whereas the other branch was connected to a spectrograph (Kymera KY328i, Andor Technology, Oxford Instruments, equipped with a 300 L mm^{-1} grating) combined with an intensified charge-coupled device (iCCD) camera (iStar iCCD-06389, Andor Technology, Oxford Instruments). The time resolved emission data were analyzed by the parallel factor analysis (PARAFAC) algorithm, using MATLAB 2021b software (The MathWorks, Inc.).

The PARAFAC algorithm deconvolutes time delay and excitation dependent emission data based on the assumption that the total measured emission is the superposition of the weighted single species emission.[32,33] This way it is possible to deconvolute the data into the luminescence decay kinetics and emission spectra of each ytterbium species. Deconvolution using a monoexponential constraint in the time dimension was done by the procedure described by.[34] The term "species" describes groups of ytterbium ions located in identical lattice sites, yielding the same emission spectrum and decay kinetics. In case of a distribution with only minimal different lattice sites, PARAFAC will fuse those into a single species with an average emission spectrum or decay kinetics. The number of species present is judged by the core consistency value. The TRES results of the ceria–Yb mixed oxides samples are two-dimensional (delay-emission tensor) and were deconvoluted in one global function thus, no reasonable core consistencies were calculated in these cases.

Results and discussion

Basic characterization of $Ce_{1-x}Yb_xO_2$ nanomaterial

TEM. The morphology of the powders was analyzed by TEM. TEM micrographs for as-synthesized CeO_2:Yb^{3+} nanoparticles are shown in Fig. 1. The micrographs display nano-sized single particles, highly monodisperse, which are spherical in shape. With the increase of the Yb^{3+} concentration, the sizes of the nanoparticles decrease only slightly. These materials were further used and annealed at 773 K as well as 1273 K.

XRD. Fig. 2 shows the X-ray diffraction patterns of low concentration Yb^{3+}–ceria (set 1, left) and high concentration Yb^{3+}–ceria samples (set 2, right) annealed at $T = 773$ K and 1273 K, respectively. For all samples six diffraction peaks are observed. Calculations using the Debye–Scherrer equation (eqn (1)) show that the crystallite size decreased inversely with the Yb^{3+} concentration in the samples (see Table 1). Additionally, a minor shift to lower 2θ values of the peak at 28.57° (for $Ce_{0.996}Yb_{0.004}O_2$) with the increase in Yb^{3+} concentration is observed. For $T = 773$ K, broader peaks are found indicating a smaller crystallite size in these samples compared to the higher annealing temperature. As an example, for the influence of the annealing temperature, for the lowest Yb^{3+}–ceria nanoparticles, the value of FWHM for the first peak decreased by a factor of five from 0.73 to 0.14 (see Table 1). Thus, an increase of the annealing temperature to 1273 K caused a substantial increase in crystallite size, suggesting melting and formation of larger aggregates in the crystal lattice. Although all the powders annealed at 1273 K were well crystallized (Fig. 2), there was no appearance of any peaks related to an isolated Yb^{3+}-phases. Diffraction peak positions of all samples match with standard diffraction positions of cubic fluorite CeO_2:Yb (standard card PDF 98-018-2971). Based on the Debye–Scherrer equation, the crystallite size of the nanomaterials decreases by 33% comparing nanomaterials of set 1 and set 2 (as shown in Table 1). With the increase in calcination temperature to 1273 K, the

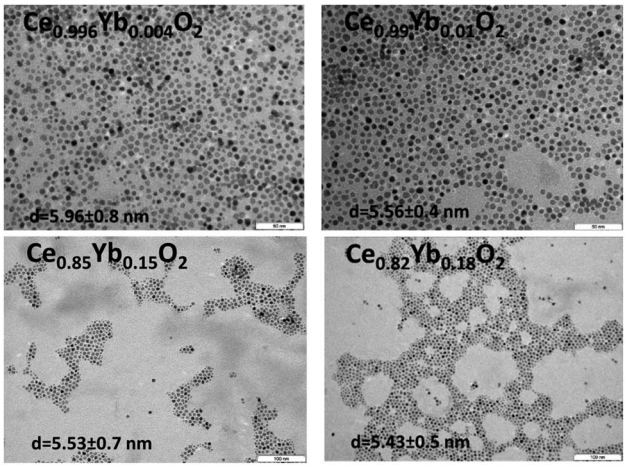

Fig. 1 TEM micrographs for as-synthesized $Ce_{1-x}Yb_xO_2$ nanomaterials. The particles sizes of the as-synthesized nanoparticles were determined to be 6 ± 1 nm.

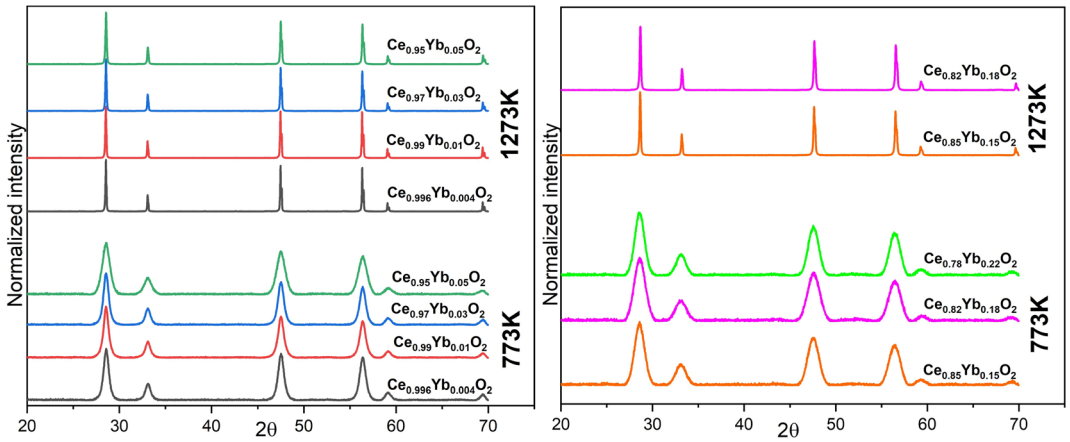

Fig. 2 XRD patterns of the 773 K and 1273 K annealed $Ce_{1-x}Yb_xO_2$ nanomaterials ($x = 0.004$, 0.01, 0.03 and 0.05) (set 1, left) and for ($x = 0.15$, 0.18 and 0.22) (set 2, right).

diffraction patterns slightly moved toward the higher 2θ values, which is in accordance with reports on the same nanomaterials synthesized by Florea *et al.*[12]

The lattice parameter for the lowest Yb^{3+} concentration (0.04 mol%) was calculated to be 0.5416 nm, but it varied from 0.5417 nm (for 1 mol% Yb–ceria) to 0.5412 nm (for 5 mol% Yb–ceria), as calculated from eqn (2) and (3). The difference in the lattice parameter shift can be directly related to the ionic radii of the dopant as compared to the host. There is a slight decrease in lattice parameter by introducing more Yb^{3+} ions in the host ion. The results are consistent with that observed by Babu *et al.* and supports that doping smaller trivalent ions *e.g.* Yb^{3+} (ionic radius 0.0985 nm) in ceria results in its lattice contraction. The extent of the lattice parameter change depends on the concentration of the trivalent dopant ion.[35] Our results are also in line with what was observed by Giannici *et al.*, where lattice contraction occurs with Yb^{3+} ion mixing into CeO_2.[36] However, Matović *et al.* observed an increase in the lattice parameters from a Yb^{3+} ions mixing concentration range of 5% to 20%.[4]

The effect of the higher annealing temperature on the samples is corroborated by the morphology results from SEM examinations (Fig. SI1†). No (significant) differences between set 1 and set 2 are found in XRD patterns, which indicate that no additional phase due to high Yb^{3+} ions content is formed or that would point to clustering of Yb^{3+} in the lattice.

Raman spectroscopy. Raman data to determine the anion ordering in the samples were collected complementary to XRD data. Fig. 3 (top) shows the Raman spectra of 773 K annealed ceria nanomaterials with increasing Yb^{3+} concentration from 0.04 to 22 mol% (both sets).

Four vibrational modes are observed in the Raman spectra. These are around 268, 464, 560, and 610 cm^{-1}, respectively. The prominent peak at 464 cm^{-1} corresponds to the triply degenerate F_{2g} Raman active mode of the fluorite structure. It is viewed as a symmetric breathing mode of the oxygen atoms around cerium ions.[11] This peak is slightly blue shifted and becomes progressively broader (see FWHM in Table 2) and asymmetric with an increase in Yb^{3+} concentration. The intensity of the two modes that appear around 560 and 610 cm^{-1} (referred to as *T* and *C* respectively) gain intensity with increasing the Yb^{3+} concentration in the samples.

These defect modes are assigned to extrinsic vacancies induced by Yb^{3+} doping and the presence of Ce^{3+}, respectively.[3] As a consequence a substantial amount of oxygen vacancies due to charge compensation is introduced in the materials as the amount of Yb^{3+} increases as also reported by Florea *et al.*[12] A very weak Raman mode around 268 cm^{-1} can be seen for the samples of set 2 heated at 773 K. Annealing at 1273 K intensifies this peak and result in the red shift of this mode to around 250 cm^{-1}.

Table 1 Crystallite size and lattice parameter of set 1 and set 2 at the two annealing temperatures with increasing Yb^{3+} concentration

Sample	Size (nm)		Peak position (°)		FWHM (°)		
Annealing temperature	773 K	1273 K	773 K	1273 K	773 K	1273 K	Lattice parameter (nm)
$Ce_{0.996}Yb_{0.004}O_2$	12.4 ± 0.2	78.7 ± 2.3	$28.57 \pm 1.2 \times 10^{-3}$	$28.54 \pm 6.1 \times 10^{-4}$	0.73 ± 0.0029	0.14 ± 0.0015	$0.5416 \pm 1.8 \times 10^{-4}$
$Ce_{0.99}Yb_{0.01}O_2$	12.5 ± 0.2	71.6 ± 1.8	$28.60 \pm 2.0 \times 10^{-3}$	$28.53 \pm 6.4 \times 10^{-4}$	1.42 ± 0.0048	0.15 ± 0.0015	$0.5417 \pm 1.8 \times 10^{-4}$
$Ce_{0.97}Yb_{0.03}O_2$	12.4 ± 0.2	40.5 ± 1.0	$28.56 \pm 9.5 \times 10^{-4}$	$28.55 \pm 5.4 \times 10^{-4}$	0.73 ± 0.0023	0.16 ± 0.0013	$0.5414 \pm 2.5 \times 10^{-4}$
$Ce_{0.95}Yb_{0.05}O_2$	9.4 ± 0.2	36.7 ± 0.7	$28.56 \pm 1.4 \times 10^{-3}$	$28.55 \pm 5.1 \times 10^{-4}$	1.02 ± 0.0033	0.17 ± 0.0012	$0.5412 \pm 2.1 \times 10^{-4}$
$Ce_{0.85}Yb_{0.15}O_2$	8.0 ± 0.3	40.7 ± 0.6	$28.58 \pm 1.7 \times 10^{-3}$	$28.65 \pm 3.3 \times 10^{-4}$	1.29 ± 0.0041	$0.18 \pm 7.7 \times 10^{-4}$	—
$Ce_{0.82}Yb_{0.18}O_2$	7.6 ± 0.3	40.0 ± 0.6	$28.55 \pm 1.1 \times 10^{-3}$	$28.67 \pm 3.1 \times 10^{-4}$	0.74 ± 0.0026	$0.18 \pm 7.4 \times 10^{-4}$	—
$Ce_{0.78}Yb_{0.22}O_2$	8.0 ± 0.2	—	$28.59 \pm 1.6 \times 10^{-3}$	—	$1.24 \pm 3.7 \times 10^{-3}$	—	—

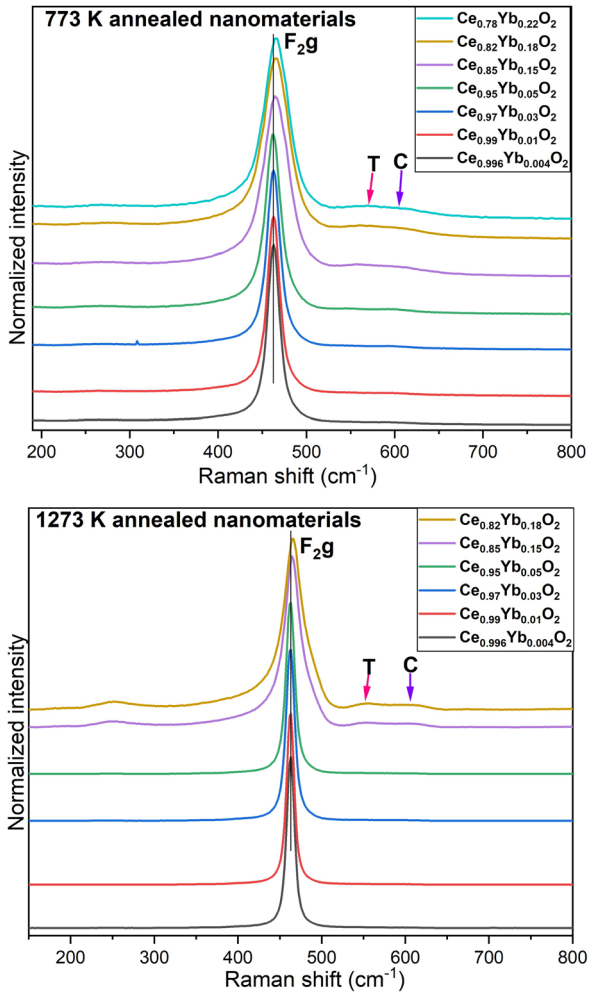

Fig. 3 Raman spectra of ceria nanomaterials annealed at 773 K (top) and at 1273 K (bottom) with increasing Yb^{3+} concentration from 0.04 to 22 mol%. (λ_{laser} = 633 nm).

Table 2 Yb^{3+} doping and calcination temperature effect on the F_{2g} Raman mode of CeO_2

Sample	FWHM (cm^{-1})	
Annealing temperature	773 K	1273 K
$Ce_{0.996}Yb_{0.004}O_2$	20.5 ± 0.2	12.8 ± 0.1
$Ce_{0.99}Yb_{0.01}O_2$	20.6 ± 0.2	12.4 ± 0.1
$Ce_{0.97}Yb_{0.03}O_2$	22.3 ± 0.2	14.4 ± 0.1
$Ce_{0.95}Yb_{0.05}O_2$	26.6 ± 0.3	14.4 ± 0.1
$Ce_{0.85}Yb_{0.15}O_2$	42.0 ± 0.6	32.0 ± 0.4
$Ce_{0.82}Yb_{0.18}O_2$	42.0 ± 0.0	36.7 ± 0.4
$Ce_{0.78}Yb_{0.22}O_2$	41.2 ± 0.6	—

As shown in Table 1, annealing the nanomaterials at 1273 K promotes the increase in the crystalline size. This might lead to the noticeable decrease in the FWHM of the F_{2g} peak of the Raman spectra with annealing temperature, as shown in Table 2 and Fig. 3 (bottom). A slight blue shift in the F_{2g} peak is also observed with the higher calcination temperature.

SEM. The topography of the nanomaterials was analyzed by SEM. The micrographs of $Ce_{1-x}Yb_xO_2$ powders are presented in Fig. SI1† (773 K, left column and 1273 K, right column). The SEM micrographs for 773 K annealed Yb^{3+}–ceria samples display that the nanomaterials have an irregular shape, have fissures and rough surfaces. The microstructural observation of the 1273 K annealed powder of set 1 shows distinct agglomeration of individual crystals (especially seen for low Yb^{3+} content). The micrographs established in some parts that there is formation of clean grains with distinct grain boundaries, to demonstrate that the grains are roughly equiaxial and condensed (can be clearly seen in the 1273 K annealed $Ce_{0.996}Yb_{0.004}O_2$ sample). With higher Yb^{3+} concentration, the surface becomes smoother and the fissures becomes less distinct, especially for the high annealing temperature.

Elemental analysis. Elemental analysis was done to determine the elemental compositions of the samples (only cerium, oxygen and ytterbium are seen in the EDX spectra). The results are shown for $Ce_{0.97}Yb_{0.03}O_2$ and $Ce_{0.85}Yb_{0.15}O_2$ annealed at 1273 K in Fig. 4. The ratios of Ce, Yb, O is nearly consistent with the nominal composition used in the synthesis.

Fig. 5 shows the elemental maps for $Ce_{0.97}Yb_{0.03}O_2$ and $Ce_{0.82}Yb_{0.18}O_2$ nanomaterials annealed at 773 K and 1273 K, respectively. Those for the $Ce_{1-x}Yb_xO_2$ (x = 0.04 and 0.15) nanomaterials are shown in the Fig. SI2.† The maps display homogeneous distribution of the ytterbium atoms in the ceria matrix for low Yb^{3+} contents (set 1 annealed at 773 K) and appear homogeneous for set 1 and 2 annealed at 1273 K. In case of set 2 samples annealed at 773 K high concentration areas are observed in some parts of the maps, which point to Yb^{3+} clusters. It is interesting to note that when the samples are annealed at 1273 K, the clusters are destroyed, which goes in line with the luminescence results (*vide infra*) and those obtained by Oliva *et al.*[17] On the other hand, XRD did not indicate the formation of clusters.

Luminescence spectroscopy of nanomaterials $Ce_{1-x}Yb_xO_2$ with low Yb^{3+} content ($x \leq 0.05$, set 1). The emission spectra of the samples were collected at room temperature and at cryogenic conditions. Fig. 6 shows the emission spectra of 773 K annealed samples.

Nine broad peaks are observed at room temperature (top) in the NIR region (a list of peak position obtained from Gaussian fitting is given in the ESI†). The manifold corresponds to the Stark levels of the $^2F_{5/2} \rightarrow {}^2F_{7/2}$ transition of Yb^{3+} ions in different environments.[19,27] There are two dominant peaks, the 972 nm and that around 976 nm. Based on the position of the emission lines, it can be hypothesized that the Yb^{3+} ions are located in C_{3v}, and C_{4v} symmetry environments, in the samples. These findings have been found in CaF_2:Yb^{3+} samples.[20–22] These symmetries are possible locations for Yb^{3+} ions in the ceria matrix due to defects sites or lattice distortions when the Yb^{3+} ions replace some of the cerium ions in the lattice. The intensity of the peak around 972 nm increases significantly as the concentration in Yb^{3+} increases from 1 to 5 mol%. The opposite happens with the intensity of the 976 nm peak. At room temperature, the homogeneous and inhomogeneous

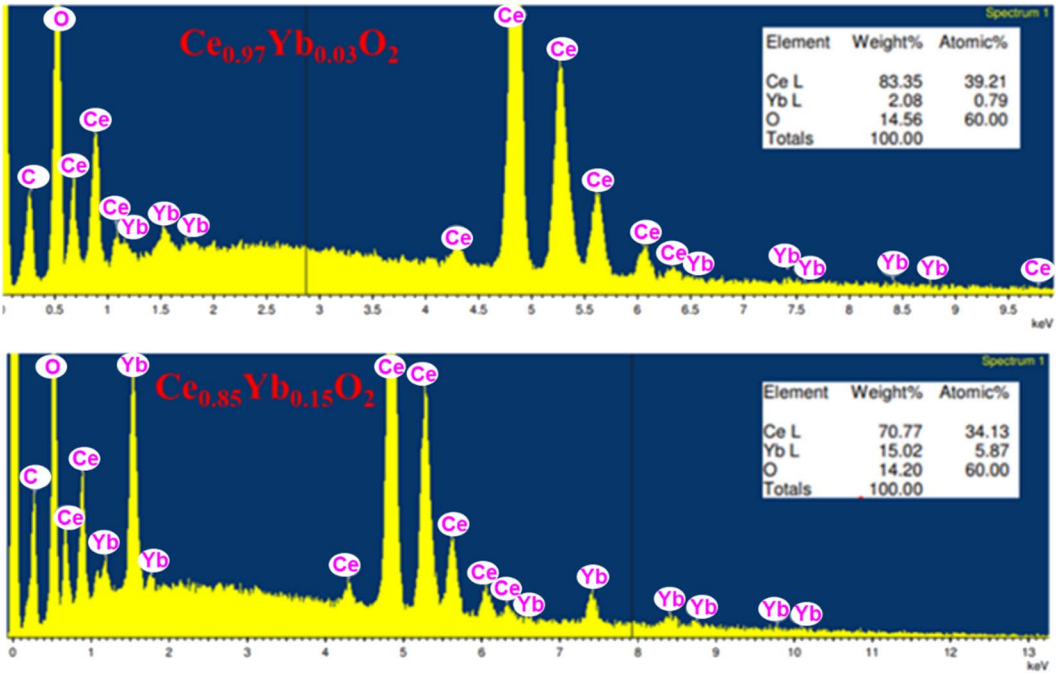

Fig. 4 EDX spectrum and elemental composition chart for $Ce_{0.97}Yb_{0.03}O_2$ and $Ce_{0.85}Yb_{0.15}O_2$ annealed at 1273 K.

broadenings in the spectral emission are strong, thus the transition between sub-levels is not totally resolved especially for peaks in the high NIR wavelengths. Thermal vibrations within the lattice could also account for the background observed, but further analysis is needed to confirm its origin.

Fig. 6 (bottom) shows that at 4 K, the peaks in the emission spectra become sharper and better resolved as homogeneous and inhomogeneous broadenings are effectively reduced. The peaks at around 972 nm and around 1028 nm become more intense with cooling, especially for the lowest Yb^{3+} concentration containing sample. Also, the 976 nm peak intensity is effectively reduced as compared to the room temperature results. In comparison with the emission spectra at room temperature, the 972 nm is slightly red shifted and the 976 nm peak slightly blue shifted as a result of cooling. This can imply that as minor adjustments of the local environment around Yb^{3+} occur, polarizability of the ligands slightly change. It can be confirmed that the 976 nm peaks belong to the C_{3v} symmetry.[20,22] The small shifts observed are induced by the changes of the crystal field around the Yb^{3+} ions.

The emission spectra of $Ce_{1-x}Yb_xO_2$ nanocrystals ($x \leq 0.05$) after annealing at 1273 K collected at room temperature (left) and at 4 K (right) are illustrated in Fig. 7. The shape of the emission spectra (*e.g.*, number of emission peaks) changes with annealing temperature. At room temperature, the 972 nm peak is most prevalent and is observed along with two broad peaks as

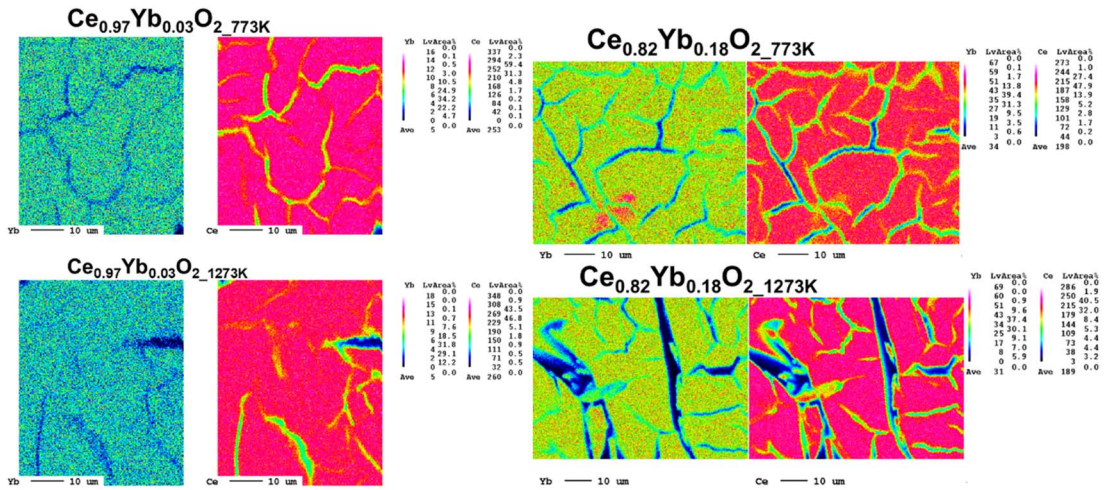

Fig. 5 Elemental maps for $Ce_{0.97}Yb_{0.03}O_2$ and $Ce_{0.82}Yb_{0.18}O_2$ nanomaterials annealed at 773 K and 1273 K for 2 h.

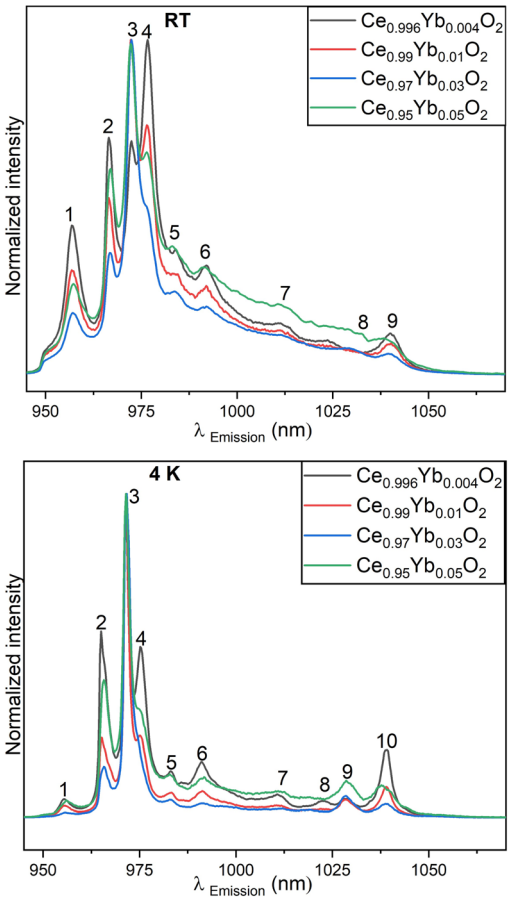

Fig. 6 Normalized emission spectra of 773 K annealed nanoparticles collected at $T = 295$ K (top) and $T = 4$ K (bottom). The Yb^{3+} luminescence was excited at $\lambda_{excitation} = 915$ nm. The delay after the laser pulse was 5 μs and the gate width used was 100 μs.

well as shoulder peaks between 950 nm and 970 nm. The most dominant peak is blue shifted and the FWHM increases with the increase of the Yb^{3+} ions amount (see Table 3). Lattice distortion is removed as crystallite growth is promoted with the higher annealing temperature resulting in the enhancement of the luminescence. Due to the position of the emission peaks and the Stark splitting pattern it is likely that the Yb^{3+} ions are located in C_{4v} and C_{3v} symmetry environments like in the room temperature results, although the peak positions are slightly shifted.[20]

The emission spectra of 1273 K annealed samples measured at 4 K again show sharper peaks compared to the spectra measured at room temperature (see Fig. 7, right). This is because the processes contributing to the spectral broadening of electronic transitions are reduced. The main feature in the emission spectra is the relatively sharp band around 972 nm. This peak is blue shifted with the increase in the Yb^{3+} ion concentration and red shifted with respect to the room temperature data. Although the peaks are narrower than those from room temperature measurements, it is still observed that there is an increase in the FWHM, with an increase in the concentration of Yb^{3+} ions (*vide infra*). Also, the 1028 nm peak is

Table 3 FWHM of the luminescence peak at 976 nm of $Ce_{1-x}Yb_xO_2$ nanomaterials ($x \leq 0.05$) annealed at 1273 K measured at RT and at 4 K and FWHM of the luminescence of the dominant peaks of the nanomaterials ($x \geq 0.15$) annealed at 773 K and 1273 K

	$FWHM_{976}$ (nm)		$FWHM_{dominant\ peak}$ (nm)	
Sample	RT_773	4 K_773	RT_1273	4 K_1273
$Ce_{0.996}Yb_{0.004}O_2$	—	—	5.8 ± 0.1	1.8 ± 0.0
$Ce_{0.99}Yb_{0.01}O_2$	—	—	6.1 ± 0.1	2.0 ± 0.0
$Ce_{0.97}Yb_{0.03}O_2$	—	—	7.4 ± 0.2	2.1 ± 0.0
$Ce_{0.95}Yb_{0.05}O_2$	—	—	9.3 ± 0.3	3.0 ± 0.8
$Ce_{0.85}Yb_{0.15}O_2$	12.1 ± 0.6	12.4 ± 0.2	4.5 ± 0.1	3.9 ± 0.2
$Ce_{0.82}Yb_{0.18}O_2$	15.7 ± 0.7	12.7 ± 0.1	4.7 ± 0.1	3.9 ± 0.2
$Ce_{0.78}Yb_{0.22}O_2$	16.7 ± 1.1	12.8 ± 0.1	4.8 ± 0.2	4.5 ± 0.3

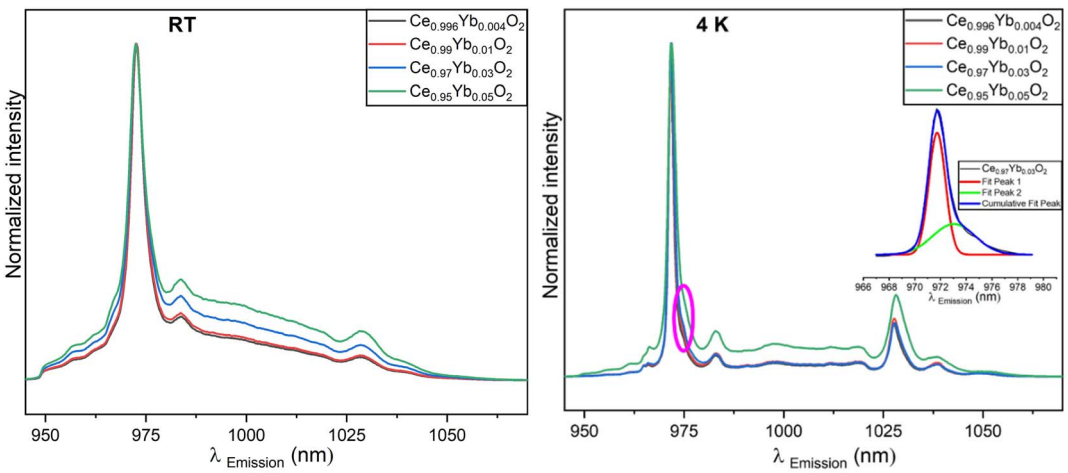

Fig. 7 Emission spectra of $Ce_{1-x}Yb_xO_2$ nanomaterials (set 1, $x \leq 0.05$) annealed at 1273 K and measured at room temperature (left) as well as at 4 K (right). A shoulder on the emission spectra around 976 nm is circled. The Gauss deconvoluted fit for nanoparticles with 3 mol% Yb^{3+} is displayed as an inset showing that two sub-peaks (fit peak 1 and 2) can be extracted. These peaks have a maximum at 971.7 nm and 973 nm respectively. The luminescence was excited at $\lambda_{excitation} = 915$ nm. The delay after the laser pulse was 5 μs and the gate width used was 100 μs.

red shifted as the concentration of the Yb^{3+} ions increase in the samples. This may be a result of a mild modification of the local environment around Yb^{3+}.[37] The peaks around 967 nm are better resolved, too (see Fig. 7, left and right, respectively). There appears to be a shoulder around 976 nm (circled) that is protruding especially for samples with 0.4, 1 and 3 mol% Yb^{3+} ions. The Gauss deconvoluted fit for $Ce_{0.97}Yb_{0.03}O_2$ displayed as an inset in Fig. 7 (right) shows that two sub-peaks can be fitted in the original 972 nm peak. These curves have a maximum at 971.7 and 973 nm respectively.

Luminescence kinetics and PARAFAC analysis $Ce_{1-x}Yb_xO_2$ nanomaterials with (set 1, $x \leq 0.05$). The time-resolved emission data were evaluated using parallel factor analysis (PARAFAC). The PARAFAC analysis yielded the separated emission spectra and the luminescence decay times of the respective homogeneous group of Yb^{3+} ions that are found on defined, isosymmetric lattice sites in ceria, herein referred to as Yb^{3+} species (Sp1–Sp3, see Fig. 8) present in set 1. Fig. 8 shows the RT (left) and 4 K (right) emission spectra PARAFAC results of 773 K annealed nanomaterials.

For room temperature three species were determined to be present in set 1 samples. The emission spectra are composed of broad peaks. The luminescence decay times for the species Sp1 and Sp2 are 583.2 μs and 1324.5 μs respectively. Species Sp3 has the least relative emission contribution and thus the determination of the respective decay time very inaccurate. Based on the emission peak pattern, Sp3 can be assigned to Yb^{3+} ions occupying a trigonal symmetry environment. On the other hand, for species Sp1 and Sp2 the C_{4v} and C_{3v} symmetries are assigned based on the location of emission peaks observed for CaF_2:Yb^{3+} ceramics.[21–23,38]

Yb^{3+} ions in three different chemical environments are seen after cooling the samples to 4 K (Fig. 8, right) as well. The spectra display sharper, better resolved, and more intense signals compared to room temperature data. Moreover, the peaks also show a blue shift (as also seen in the raw data). Although, the spectrum from species Sp3 has a shoulder around 976 nm, the peaks around 1040 nm are well resolved and clearly seen. The luminescence decay time of species Sp2 is longest (1992.2 μs), which might be an indication for a slow rate of energy migration between the isolated Yb^{3+} ions.[25] Sp1 has a decay time of 545.3 μs. Also, in this case the relative emission contribution of species Sp3 is low. However, as it is seen (*vide infra*), this species becomes the main species after annealing the nanomaterial samples at a higher temperature. As in the RT results, Yb^{3+} ions assigned to species Sp3 could be located in a C_{3v} environment, while the other Yb^{3+} ions represented by species Sp2 and Sp1 are assigned with more confidence to C_{4v} and C_{3v} symmetry environments since they dominate in the luminescence.[20,22] More research on the down conversion in ceria-based nanomaterials mixed with Yb^{3+} should be done to be able to confirm the assignment of the emission peaks in these materials.

The emission spectra from PARAFAC results of room temperature and 4 K luminescence measurements of 1273 K annealed samples are shown in Fig. 9. PARAFAC deconvoluted RT data showed only one Yb^{3+} species present which portrays homogeneity and high crystallinity in the samples due to annealing at a higher temperature (see Fig. 9).

A broad spectrum with a main peak centered around 972 nm is observed at room temperature together with a shoulder at *ca.* 967 nm and three more small peaks. The peaks become sharper with cooling to cryogenic conditions and the shoulder (in room temperature result that is around 967 nm) is well separated now into two peaks (although small) and the other peaks are also better resolved and more intense. Furthermore, the main peak is blue shifted. Also, upon cooling, the luminescence decay kinetics became slower indicated by the increased luminescence decay time (441.7 μs and 612.4 μs at RT and at 4 K respectively). For the samples annealed at 1273 K the Yb^{3+} ions are assumed to be in tetragonal and trigonal symmetry environments.[22] Species Sp3 (RT, Fig. 8, left) and Sp3 (4 K, Fig. 8, right) of samples annealed at 773 K PARAFAC analysis yielded an emission profile which resembles that for single species found in the 1273 K annealed samples.

Luminescence of $Ce_{1-x}Yb_xO_2$ (set 2, $x \geq 0.15$) nanomaterials. Fig. 10 shows the emission spectra of 773 K and 1273

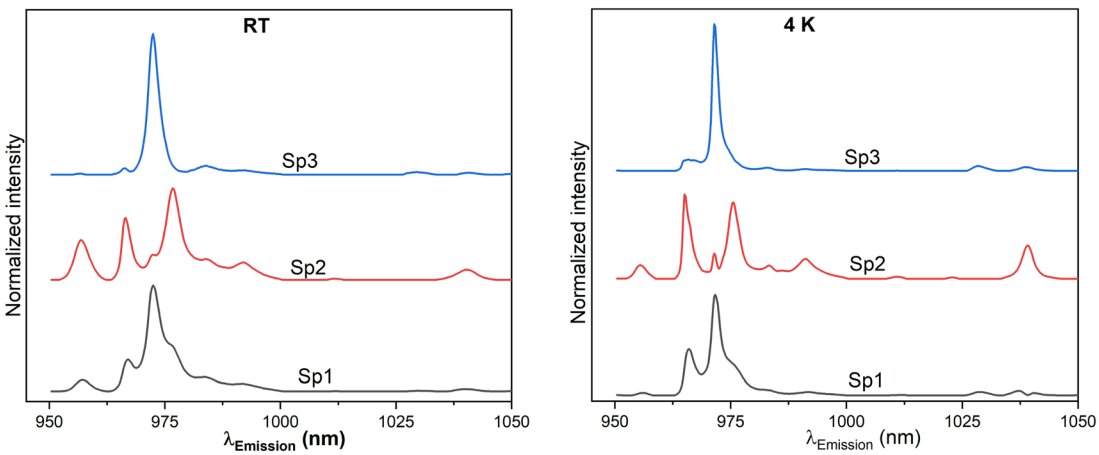

Fig. 8 Emission spectra from RT (left) and 4 K (right) 773 K annealed nanomaterials obtained from PARAFAC results. For the luminescence measurements, $\lambda_{excitation} = 915$ nm. The delay after the laser pulse was 5 μs and the gate width used was 100 μs.

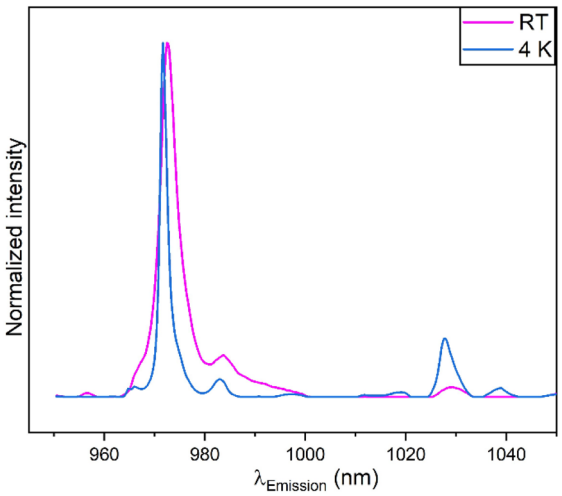

Fig. 9 Emission spectra of room temperature and 4 K measured 1273 K annealed samples (set 1, $x \leq 0.05$) obtained from PARAFAC analysis.

K annealed $Ce_{1-x}Yb_xO_2$ ($x \geq 0.15$) nanomaterials measured at room temperature and at cryogenic conditions. The $^2F_{5/2} \rightarrow {}^2F_{7/2}$ emission is observed.[39] The spectra consist of two broad peaks with the 976 nm peak being the most prevalent. The FWHM of the dominant peak in each sample is displayed in Table 3. In the luminescence measurements of set 2, a strong background emission was observed for all samples of which the origin is not clear. The overall appearance is hypothesized as the overlay of spectra from Yb^{3+} ions which are in the close vicinity of each other (possible in slightly different environments) leading to distinct peak broadening. Strong emission at 976 nm reveals self-absorption of Yb^{3+} ions in the nanomaterials.[19,40] Also, as Yb^{3+} concentration increases, there is a high chance that more Yb^{3+}–Yb^{3+} clusters are formed thereby reducing the emission of isolated Yb^{3+} ions.[27] Elemental mapping (Fig. 5) corroborates this fact (*vide supra*). Contribution of the Yb^{3+} clusters increases and the peaks in the emission spectra broaden. As a result, the distinction between the purely electronic and vibronic transitions is not clear cut. Cooling the samples down to 4 K does not result in sharper peaks in the emission signals because energy transfer between the Yb^{3+} ions is not eliminated. The two peaks are noticeably red shifted (the most dominant peak from about 976 nm to 980 nm). These peaks are also better separated compared to room temperature results.

Annealing the nanomaterials at 1273 K results in the spectral signature changes as new peaks emerge at (983 and 1028 nm), with the most prevalent peak around 972 nm, all becoming slightly sharper after cooling to cryogenic conditions. The peaks also become well separated and a shoulder peak around 976 nm is observed, which is also observed for set 1 heated at 1273 K and the emission measured after cooling to 4 K (*vide supra*). Also, cooling to 4 K induces a blue shift on the dominant peak. A shoulder around 976 nm at emission profiles for room temperature measured samples is seen. Overall, for this set of samples the Yb^{3+} ions are assumed to be located in low symmetry environments based on their emission data. In Table 3, the FWHM of the dominant peak of the oxides is shown. A decrease of the FWHM of the dominant peaks is observed after (i) annealing the oxides at 1273 K and (ii) after cooling down the samples to 4 K for the luminescence measurements.

PARAFAC analysis. The emission spectra based on room temperature and 4 K luminescence measurements of 773 K and 1273 K annealed samples obtained from PARAFAC analysis are shown in Fig. 11 (left and right, respectively).

PARAFAC deconvoluted data (room temperature as well as 4 K) for 773 K annealed samples (Fig. 11, left) reveal only one Yb^{3+} species. The determined emission spectra have a broad dominant 978 nm peak along with another broad smaller peak centered at around 1012 nm (very similar to the raw data). The emission profile resembles that of a hexameric cluster that has been identified for CaF_2:Yb^{3+} crystals with high content of Yb^{3+} ions.[20,22] The luminescence of this species is greatly quenched judged by its luminescence decay time of only 2 μs. This is due to cross-talk between excited Yb^{3+} in close vicinity leading to energy migration among Yb^{3+} ions.[41] There is no significant change observed in the PARAFAC results analyzing the 4 K data, except a slight red shift of the dominant peak. Thus, it is seen

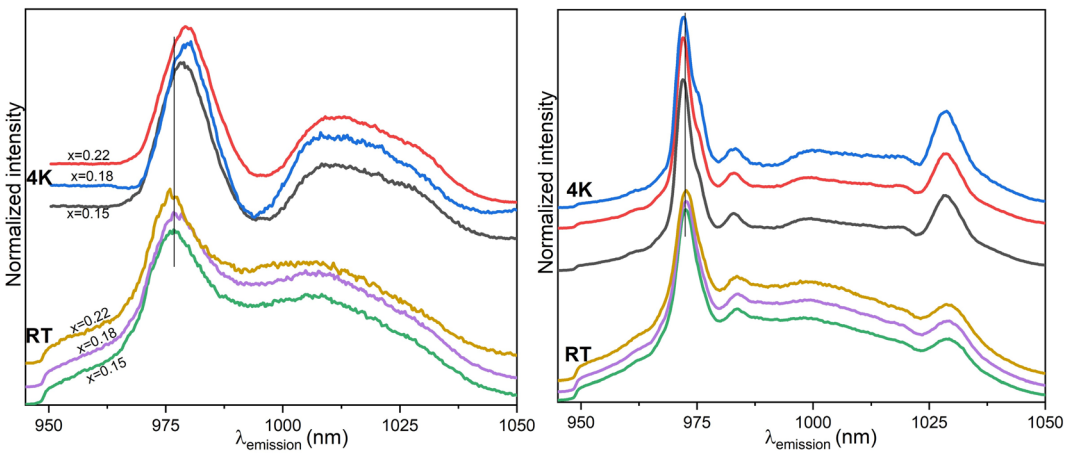

Fig. 10 Emission spectra of 773 K (left) and 1273 K (right) annealed ($Ce_{1-x}Yb_xO_2$ ($x \geq 0.15$)) nanomaterials collected at room temperature and at 4 K. $\lambda_{excitation} = 915$ nm. The delay after the laser pulse was 5 μs and the gate width used was 100 μs.

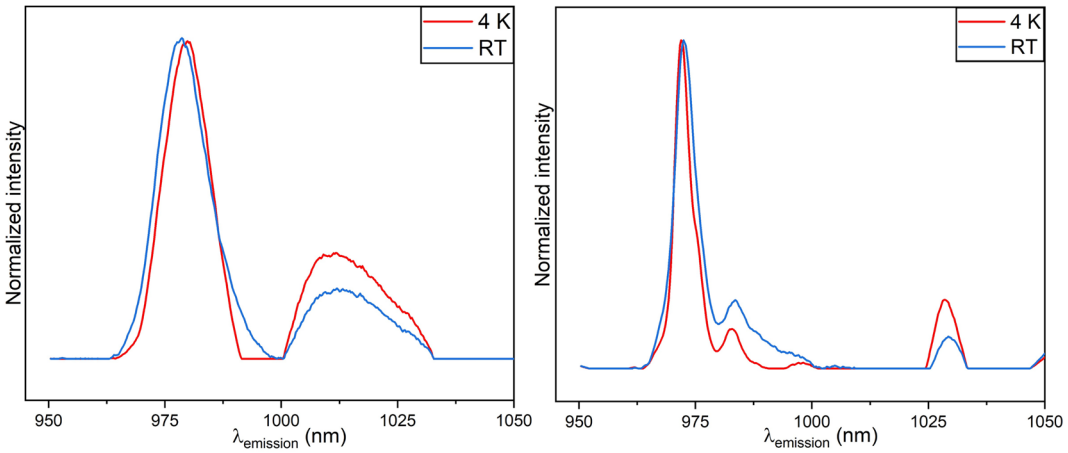

Fig. 11 Emission spectra of 773 K annealed $Ce_{1-x}Yb_xO_2$ ($x = 0.15$, 0.18 and 0.22) oxides PARAFAC results of luminescence measurements done at RT (blue) and at 4 K (red) (left) and of 1273 K annealed $Ce_{1-x}Yb_xO_2$ ($x = 0.15$, 0.18 and 0.22) mixed oxides PARAFAC results of analyses done at RT and at 4 K (right).

that when concentrations are elevated, as opposed to set 1, samples show short luminescence decay times, signifying a turning point for Yb^{3+}, shifting from singly isolated state to clusters.[25] Therefore, it is only sensible to reiterate the fact put out by Tamrak *et al.* that as Yb^{3+} concentration increases, additional Yb^{3+}–Yb^{3+} pairs are formed, promoting cluster formation thus plummeting the emission of single Yb^{3+} ions.[27] The emission spectra of set 2 annealed at 1273 K obtained by PARAFAC analysis for luminescence measurements carried out at RT and at 4 K are displayed in Fig. 11 (right). For the oxides annealed at 1273 K also only one Yb^{3+} species was found. The dominant peak in RT data is slightly blue shifted and also becomes slightly sharper with cooling (FWHM = 6.0 nm at RT and 4.82 nm at 4 K). The shoulder peak found around 992 nm is better resolved after cooling. It should be stressed that with a higher annealing temperature, the peak that dominates as a result of the so called hexameric cluster, occurring at circa 979 nm in 773 K annealed samples disappears, paving way to another new dominant peak. This also indicates a rearrangement and a destruction of the clusters with a higher annealing temperature, which is in line with the EDX results (*vide supra*). The decay times for the samples change from 44.4 μs for RT measurements to 50.4 μs for 4 K measurements (which is also significantly higher than for 773 K annealed samples and a further indication that the energy transfer between Yb^{3+} ions is reduced). It is however, interesting to note that, although the concentration of Yb^{3+} ions are very different in Yb^{3+}-doped ceria and ceria oxide nanomaterials with high Yb^{3+} concentration, the RT and 4 K luminescence spectral signatures of 1273 K annealed nanomaterials (Fig. 11, right) are similar to that from Fig. 9, depicting the similarity in the most dominant symmetry environment occurring for the Yb^{3+} ions.

Conclusions

$Ce_{1-x}Yb_xO_{2-y}:Eu^{3+}$ ($0.004 \leq x \leq 0.22$) nanomaterials were synthesized by a thermal decomposition method, with the molar quantities supported by EDX analysis. The particle crystallites of the 773 K and 1273 K annealed nanomaterials are nano-sized and have a cubic fluorite structure with four Raman vibrational modes as revealed by the XRD data and Raman spectroscopy data, respectively. Elemental maps clearly show that cluster formation occurs with high Yb^{3+} ion concentration from 15 mol% in the ceria lattice. The emission spectra of the $Ce_{1-x}Yb_xO_{2-y}:Eu^{3+}$ ($0.004 \leq x \leq 0.05$) nanoparticles observed for room temperature and 4 K show a manifold of luminescence bands that corresponds to the $^2F_{5/2} \rightarrow {}^2F_{7/2}$ transition of Yb^{3+} ions.

Different emission spectral signatures are observed for $Ce_{1-x}Yb_xO_{2-y}:Eu^{3+}$ ($0.15 \leq x \leq 0.22$) nanomaterials, although the $^2F_{5/2} \rightarrow {}^2F_{7/2}$ transition is still detected. The emission spectra comprise of two broad high background dominated peaks. Cooling the samples down to 4 K results in small shifts observed in the Stark splitting pattern. Annealing the nanomaterials at 1273 K changes the spectral signatures as new peaks emerge and all peaks become slightly sharper and better resolved after cooling to cryogenic conditions.

PARAFAC analysis was executed to extract different Yb^{3+} species from the time-resolved luminescence data collected at RT and 4 K for both low and high concentration Yb^{3+} samples. The deconvolution yielded luminescence decay kinetics as well as the associated luminescence spectra of three species for each of the low Yb^{3+} doped ceria samples annealed at 773 K but only one species for the 1273 K annealed samples. Decay kinetics after cooling the samples to 4 K resulted in species with the decay times of 545.3 μs and 1992 μs. Annealing the nanomaterials at 1273 K and measuring the decay kinetics of the species resulted in one species with a decay time of 441.7 μs and 612.4 μs at RT and 4 K, respectively. However, the high concentration Yb^{3+} ceria samples yielded only one species with a distinctly lower decay times as compared to the low Yb^{3+} ions doped ceria samples. Here, the annealing temperature had only a small influence. As supported by elemental mapping analysis, increasing Yb^{3+} concentration in the ceria oxides, from 15 mol%

up, enhances cluster formation, thus reducing the emission of single Yb^{3+} ions. A notable increase (from 2 μs to 50 μs) in the luminescence decay time was found for set 2 samples annealed at 1273 K, which confirmed that with higher annealing temperatures clusters are removed.

On a balance of probabilities, with good data processing, the presented results on Yb^{3+} could be an adaptable and sensitive structural probe that can be used to probe samples in the NIR region that is effective in technical materials. Also, in conjunction with the PARAFAC algorithm, valuable deconvolution of the data observed in room temperature measurements and overall high-resolution data from 4 K measurements especially provide a distinction on the number of Yb^{3+} species in low and high concentration Yb^{3+} ceria samples, where many sites can contribute to the overall emission.

Author contributions

S. C. and M. U. K. conceived this project. T. S. and S. C. prepared the samples. S. C. and C. G. conducted the investigations and characterizations. S. C. and C. G. analysed the data. S. C. drafted the original manuscript. M. U. K. reviewed and edited the manuscript with contributions from all authors.

Conflicts of interest

There are no conflicts to declare.

Acknowledgements

Authors are grateful to Dr Sibylle Rüstig for help with TEM measurements and Sophie Dettmann for supporting with data processing. S. C. and M. U. K. are thankful to the Deutsche Forschungsgemeinschaft (DFG, German Research Foundation) for financial support (grant no. 450169704). M. U. K. greatly appreciates the financial support by the Federal Ministry for the Environment, Nature Conservation, Nuclear Safety and Consumer Protection (02E11860F). Publication was funded by the Deutsche Forschungsgemeinschaft (DFG, German Research Foundation) – grant no. 491466077.

Notes and references

1 A. E. D'Achille, R. Gonzalez-Rodriguez, E. Campbell, B. H. Lee, J. L. Coffer and A. V. Naumov, *ACS Biomater. Sci. Eng.*, 2020, **6**, 6971–6980.
2 B. Choudhury, P. Chetri and A. Choudhury, *J. Exp. Nanosci.*, 2015, **10**, 103–114.
3 D. Avram, I. Porosnicu, B. Cojocaru, M. Florea and C. Tiseanu, *J. Lumin.*, 2016, **179**, 265–271.
4 B. Matović, M. Stojmenović, J. Pantić, A. Varela, M. Žunić, N. Jiraborvornpongsa and T. Yano, *J. Asian Ceram. Soc.*, 2014, **2**, 117–122.
5 C. Walkey, S. Das, S. Seal, J. Erlichman, K. Heckman, L. Ghibelli, E. Traversa, J. F. McGinnis and W. T. Self, *Environ. Sci.: Nano*, 2015, **2**, 33–53.
6 Y. Li, Y. Li, H. Wang and R. Liu, *ACS Appl. Mater. Interfaces*, 2021, **13**, 13968–13977.
7 M. A. Małecka, *CrystEngComm*, 2017, **19**, 6199–6207.
8 D. Han, Y. Yang, F. Gu and Z. Wang, *J. Alloys Compd.*, 2016, **656**, 524–529.
9 C. L. Muhich, *J. Phys. Chem. C*, 2017, **121**, 8052–8059.
10 A. Kumar, S. Babu, A. S. Karakoti, A. Schulte and S. Seal, *Langmuir*, 2009, **25**, 10998–11007.
11 S. Chemura, T. Haubitz, P. A. Primus, M. Underberg, T. Hülser and M. U. Kumke, *J. Phys. Chem. A*, 2020, **124**, 4972–4983.
12 M. Florea, D. Avram, V. A. Maraloiu, B. Cojocaru and C. Tiseanu, *Nanoscale*, 2018, **10**, 18043–18054.
13 G. Boulon, *J. Alloys Compd.*, 2008, **451**, 1–11.
14 L. Liu, J. Xing, F. Shang and G. Chen, *Opt. Commun.*, 2021, **490**, 126944.
15 J. Chen and J. X. Zhao, *Sensors*, 2012, **12**, 2414–2435.
16 A. Kaminska, J. Cybińska, Y. Zhydachevskii, P. Sybilski, G. Meyer and A. Suchocki, *J. Alloys Compd.*, 2011, **509**, 7993–7997.
17 J. Oliva, E. De la Rosa, L. Diaz-Torres, P. Salas and C. Ángeles-Chavez, *J. Appl. Phys.*, 2008, **104**, 023505.
18 H. Zhang, Z.-H. Chen, X. Liu and F. Zhang, *Nano Res.*, 2020, **13**, 1795–1809.
19 Z. Zou, Y. He, H. Yu, S. Pang, Y. Wu, J. Liu and L. Su, *Opt. Mater. Express*, 2018, **8**, 1747–1753.
20 V. Petit, P. Camy, J.-L. Doualan, X. Portier and R. Moncorgé, *Phys. Rev. B: Condens. Matter Mater. Phys.*, 2008, **78**, 085131.
21 Y. K. Voron'Ko, V. Osiko and I. Shcherbakov, *J. Exp. Theor. Phys.*, 1969, **29**, 86–90.
22 T. Kallel, M. A. Hassairi, M. Dammak, A. Lyberis, P. Gredin and M. Mortier, *J. Alloys Compd.*, 2014, **584**, 261–268.
23 J. Kirton and S. McLaughlan, *Phys. Rev.*, 1967, **155**, 279.
24 W.-P. Qin, Z.-Y. Liu, C.-N. Sin, C.-F. Wu, G.-S. Qin, Z. Chen and K.-Z. Zheng, *Light: Sci. Appl.*, 2014, **3**, e193.
25 S. Mei, J. Zhou, H. T. Sun, Y. Cai, L. D. Sun, D. Jin and C. H. Yan, *Adv. Sci.*, 2021, **8**, 2003325.
26 G. Lakshminarayana, H. Yang, S. Ye, Y. Liu and J. Qiu, *J. Phys. D: Appl. Phys.*, 2008, **41**, 175111.
27 R. K. Tamrakar, D. Bisen, K. Upadhyay, I. P. Sahu and N. Brahme, *J. Opt.*, 2015, **44**, 337–345.
28 E. Montoya, J. Sanz-García and L. Bausa, *Spectrochim. Acta, Part A*, 1998, **54**, 2081–2085.
29 Z. Chen, W. Gong, T. Chen, S. Li, D. Wang and Q. Wang, *Mater. Lett.*, 2012, **68**, 137–139.
30 J.-H. Cho, M. Bass, S. Babu, J. M. Dowding, W. T. Self and S. Seal, *J. Lumin.*, 2012, **132**, 743–749.
31 S. S. Lee, W. Song, M. Cho, H. L. Puppala, P. Nguyen, H. Zhu, L. Segatori and V. L. Colvin, *ACS Nano*, 2013, **7**, 9693–9703.
32 R. Bro and C. A. Andersson, *Chemometr. Intell. Lab. Syst.*, 1998, **42**, 105–113.
33 C. A. Andersson and R. Bro, *Chemometr. Intell. Lab. Syst.*, 2000, **52**, 1–4.
34 B. Drobot, R. Steudtner, J. Raff, G. Geipel, V. Brendler and S. Tsushima, *Chem. Sci.*, 2015, **6**, 964–972.
35 S. Babu, R. Thanneeru, T. Inerbaev, R. Day, A. E. Masunov, A. Schulte and S. Seal, *Nanotechnology*, 2009, **20**, 085713.

36 F. Giannici, G. Gregori, C. Aliotta, A. Longo, J. Maier and A. Martorana, *Chem. Mater.*, 2014, **26**, 5994–6006.
37 F. Wang, L. Hu, W. Xu, M. Wang, S. Feng, J. Ren, L. Zhang, D. Chen, N. Ollier and G. Gao, *Opt. Express*, 2017, **25**, 25960–25969.
38 M. Ito, C. Goutaudier, Y. Guyot, K. Lebbou, T. Fukuda and G. Boulon, *J. Phys.: Condens. Matter*, 2004, **16**, 1501.
39 Q. Zhang and X. Liang, *J. Soc. Inf. Disp.*, 2008, **16**, 755–758.
40 L. Xia, C. Yu, S. Sun, Q. Zhou, F. Wang, S. Wang, L. Hu, Q. Yang and Y. Zhang, *Opt. Mater.*, 2019, **98**, 109352.
41 J. Li, J. Zhang, Z. Hao, X. Zhang, J. Zhao and Y. Luo, *Appl. Phys. Lett.*, 2012, **101**, 121905.